Injection and interplanetary transport of near-relativistic electrons. Modeling the impulsive event on 2000 May 1

N. Agueda,[1] R. Vainio,[2] D. Lario,[3] and B. Sanahuja[1,4]

nagueda@am.ub.es

ABSTRACT

We present a Monte Carlo method to model the transport of solar near-relativistic electrons in the interplanetary medium, including adiabatic focusing, pitch-angle dependent scattering, and solar wind effects. By taking into account the angular response of the LEFS60 telescope of the EPAM instrument on board the *ACE* spacecraft, we transform the simulated pitch-angle distributions into the sectored intensities measured by the telescope. The goal is to deconvolve the effects of the interplanetary transport in order to infer the underlying injection profile and the radial mean free path of the electrons. We apply the model to the near-relativistic electron event observed on 2000 May 1, associated with an impulsive X-ray flare, type III radio bursts, and a narrow fast CME. The deconvolved interplanetary transport conditions reveal a long radial mean free path of 0.9 AU and pitch-angle dependent scattering. The eight observed sectored intensities are fitted in detail for more than 90 min, except for a short period ($\sim$12 min) right after the time of peak intensities. This discrepancy may suggest that the assumed scattering model performs more efficiently than the actual scattering processes at work. The resulting injection profile consists of two main components, an initial component lasting 2–3 min and probably related to a type III radio burst observed by *WIND*/WAVES at $\sim$10:21 UT, and a delayed component starting at the Sun around 10:35 UT with a typical injection decay time scale of $\sim$0.5 h. The delayed component may be related to the CME-driven shock.

Subject headings: Sun: particle emission – Sun: flares – Sun: coronal mass ejections (CMEs)

---

[1]Departament d'Astronomia i Meteorologia, Universitat de Barcelona, 08028 Barcelona, Spain

[2]Department of Physical Sciences, University of Helsinki, 00014 Helsinki, Finland

[3]Applied Physics Laboratory, The Johns Hopkins University, Laurel, MD 20723-6099, USA

[4]Institut d'Estudis Espacials de Catalunya (ICC-UB), 08028 Barcelona, Spain

1. Introduction

Near-relativistic ($E > 30$ keV) electron events observed in interplanetary space have received considerable attention since the early work of Lin (1970). These near-relativistic (NR) electrons constitute the most common type of solar energetic particle (SEP) emission (Lin 1970). Although NR electron increases are observed in association with both large and small proton events, a distinctive class of SEP events with high electron-to-proton ratios, linked to small solar flares and type III radio bursts emerged from the first analysis of these events (Lin 1970). These events, commonly classified as impulsive, have additional distinguishable characteristics such as enhanced ^{3}He/^{4}He ratios (Reames 1999, and references therein).

Two independent studies (Krucker et al. 1999; Haggerty & Roelof 2002) have indicated that in most NR electron events the inferred release time of the electrons can be delayed from the onset of the type III burst by up to half an hour. In the determination of the release time, Krucker et al. (1999) used c/v plots and assumed that the time of the release of the particles was energy independent. Scatter-free energetic particle propagation was the key assumption made by Haggerty & Roelof (2002)

In order to understand the relationship between the NR electrons detected at 1 AU and the electrons that generate the type III radio emissions several studies have invoked shock acceleration (Simnett et al. 2002), post-eruptive magnetic reconnection (Maia & Pick 2004; Klein & Posner 2005), and interplanetary transport effects (Cane 2003). Wang et al. (2006) simulated three impulsive electron events by assuming interplanetary scatter-free propagation. They derived the existence of energy dependent injections. The injection of the low-energy (∼0.4-9 keV) electrons was found to be coincident with the type III bursts emissions, whereas the high-energy (∼13-300 keV) electron injection was delayed and occurred when the associated coronal mass ejection (CME) passed ∼1-6 $R_\odot$. Recently, Kahler et al. (2007) analyzed a large sample of 80 NR electron events, studying the correlations between injection delays, solar radio emissions, and in-situ solar wind characteristics. This study confirmed median ∼10 min injection delays, and the correlation of the delays with the ambient solar wind densities measured at 1 AU. They concluded that the association between electron events with long-duration ($\geq$ 2 h) large electron anisotropies at 1 AU and type II bursts provided support for the possibility of a class of shock-accelerated NR electron events.

A plausible acceleration mechanism for particles in the solar corona accounting for electron and ^{3}He enhancements is stochastic acceleration by (weak) MHD turbulence consisting of a superposition of MHD waves (e.g. Petrosian & Liu 2004; Liu et al. 2006). In this scenario, particle acceleration is a fast process following the generation of turbulence by the

release of magnetic energy during the flare. From the analysis of large SEP events and in-situ observations in the near-Earth space, we know that also shock waves are efficient particle accelerators (see, for example, Cliver & Ling 2007). As magnetic reconnection can generate super-fast-magnetosonic flows, the presence of shocks in flares is plausible (Aurass et al. 2002). Furthermore, some impulsive flares are also accompanied by CMEs, which are very likely to be drivers of global shock waves through the corona (Kahler et al. 2001). The time scales associated with the expansion of the global coronal shock waves are of the order of hours, i.e., much longer than the typical time scales in impulsive flares.

One method for finding out about the relative importance of flare acceleration versus shock acceleration is to deduce the temporal evolution of the source emitting particles from the corona into the interplanetary medium. In order to determine the injection profile of the NR electrons measured in space, it is necessary to deconvolve the effects of particle transport from the particle acceleration sites to the spacecraft. Moreover, it is also imperative to use anisotropy measurements to correctly model the energetic particle transport conditions. In this paper, we develop a detailed transport model based on the Monte Carlo method that allows a correct description of particle propagation along interplanetary magnetic field (IMF) lines. We also introduce an algorithm suitable for analyzing sectored intensities computed by a particle telescope on board a spin-stabilized spacecraft. We apply this model to the impulsive event observed on 2000 May 1 by the LEFS60 telescope of the Electron Proton and Alpha Monitor (EPAM) on board the *Advanced Composition Explorer* (*ACE*) (Gold et al. 1998). We infer the particle injection time profiles and compare them with the solar phenomena associated with the origin of the SEP event.

We present the particle transport model in section 3. The fitting procedure applied to deconvolve the sectored intensities observed by the EPAM/LEFS60 telescope is described in section 4. In section 5, we describe the NR electron event detected on 2000 May 1. Results of the application of the model are presented and discussed in section 6. Finally, section 7 gives the conclusions of this work. Technical details about the Monte Carlo simulations of interplanetary transport and the derivation of the angular response model of the EPAM/LEFS60 sectors are given in the appendices A and B, respectively.

2. An overview of the observations

ACE is a spin-stabilized spacecraft which rotates about an axis directed within 20° of the Sun with a spin period of 12 s. The LEFS60 telescope of the EPAM experiment (Gold et al. 1998) measures energetic (0.46–4.9 MeV) ions and NR (45–312 keV) electrons in seven energy channels (four for electrons and three for ions). This telescope is pointed 60° off

the spacecraft spin axis. As the spacecraft rotates, the instrument electronics sample the detector so that the solid angle swept by the telescope is divided into eight equal sectors, each 45° wide in clock-angle. The geometric factor of the LEFS60 telescope is 0.397 cm^2 sr, with a full-cone opening angle of 53°. In this paper, we analyze 72-sec averages of the sectored electron intensities measured by the LEFS60 telescope in the energy range 62–312 keV during the impulsive SEP event on 2000 May 1. We do not include the lowest energy channel of the telescope (45–62 keV) because of possible contribution from higher energy electrons (see section 6). For completion, we also use 8-min spin-averaged 1.06–4.8 MeV proton intensities observed by the EPAM/LEMS120 telescope (Gold et al. 1998) and the 1.33–4.75 MeV proton intensities observed by the ERNE telescope on board SOHO (Torsti et al. 1995) with the same time resolution.

Magnetic field and solar wind plasma observations at 1 AU were provided by the MAG (Smith et al. 1998) and SWEPAM (McComas et al. 1998) instruments on board *ACE*. We use 72-sec averages of the magnetic field magnitude and direction. SWEPAM data are used to estimate the mean solar wind speed during the period of study and are taken at 64-sec time resolution. We also use data from the LASCO coronograph on board *SOHO* (Brueckner et al. 1995) and radio data from the WAVES experiment on board the *WIND* spacecraft (Bougeret et al. 1995), as well as X-ray fluxes from the X-Ray Sensor (XRS) on board the *GOES-8* satellite[1]. Finally, we use ground-based radio observations reported by the Solar Geophysical Data[2] (US Department of Commerce, Boulder, CO, USA).

3. The model

We have developed a Monte Carlo model to compute the interplanetary transport of SEPs injected at the root of an Archimedean spiral magnetic field line (Parker 1958). Our calculations of the particle propagation are based on the focused transport model that includes the effects of adiabatic focusing by the diverging Parker field, the interplanetary scattering by magnetic fluctuations frozen-in into the solar wind, convection with the scattering fluctuations and adiabatic deceleration resulting from the interplay of scattering and focusing (Ruffolo 1995; Kocharov et al. 1998). We include the adiabatic deceleration process for completeness although its effect on the NR electrons that we are studying is minimal.

We consider an impulsive and isotropic injection of SEPs at the distance of $2R_\odot$ from

[1]http://rsd.gsfc.nasa.gov/goes/

[2]http://sgd.ngdc.noaa.gov

the center of the Sun. We assume that the source function of SEPs is a power law in energy with spectral index γ ($\propto E^{-\gamma}$). We simulate the release of a large number of particles and the subsequent transport along an IMF line using the Monte Carlo method (Torsti et al. 1996; Kocharov et al. 1998; Vainio 1998; Maia et al. 2007). During particle propagation, we keep track of the particles in the frame corotating with the Sun, where the particle speed is approximately conserved during propagation. We move the particles in small radial Monte Carlo steps, δr. After each step, we calculate the new particle position, $r = r_0 + \delta r$, the new pitch-angle cosine due to focusing $\mu(r; r_0, \mu_0)$, and the time elapsed during the propagation, $\delta t(r, \mu; r_0, \mu_0)$. All these quantities can be analytically calculated for an Archimedean spiral magnetic field. After computing these quantities, we change the pitch-angle cosine of the particle due to scattering. The scattering is performed in the local solar wind frame, where the magnetic fluctuations are assumed to be static and, therefore, the particle speed is conserved. This change of frames of reference leads to a systematic decrease of the energy of the particle in the solar-wind reference frame as the particle moves away from the Sun (Ruffolo 1995).

In the solar wind frame, the pitch-angle diffusion coefficient can be expressed as

$$D_{\mu\mu} = \frac{\nu}{2}(1 - \mu^2), \tag{1}$$

where ν is the scattering frequency, proportional to the power spectrum of the magnetic fluctuations in the neighborhood of the resonant wave number $k = \Omega/v\mu$, where Ω is the gyrofrequency of the particle. The relation of $D_{\mu\mu}$ to the parallel scattering mean free path $\lambda_\parallel$ is given by (Hasselmann & Wibberenz 1968, 1970)

$$\lambda_\parallel = \frac{3v}{8}\int_{-1}^{1}\frac{(1-\mu^2)^2}{D_{\mu\mu}}d\mu = \frac{3v}{4}\int_{-1}^{1}\frac{1-\mu^2}{\nu(\mu)}d\mu. \tag{2}$$

It is worth to remember that $\lambda_\parallel$ is defined under two basic assumptions: slow time dependence (near stationarity) and strong scattering. Therefore, at the limit of weak scattering, the physical meaning of the $\lambda_\parallel$ parameter is questionable. A relevant discussion on this point can be found in Qin et al. (2005). Following previous studies, and with the aim at providing results directly comparable to earlier studies, we use the mean free path as the primary quantity parametrizing the scattering, even for large values of $\lambda_\parallel$. However, the actual strength of scattering in the case of long $\lambda_\parallel$ is discussed in more detail in the appendix section A.3.

We perform a particle scattering after every radial Monte Carlo step. In the case of isotropic (or pitch-angle independent) scattering, i.e. ν constant, $D_{\mu\mu}$ has a functional form of a downward-opening parabola and the mean free path is given by $\lambda_\parallel = v/\nu$. A simple and efficient method to model isotropic pitch-angle diffusion in a Monte Carlo simulation is to

consider an ensemble of particles, all starting from a given point in phase space. After a given time $\delta t \ll \nu^{-1}$, the distribution of particles around the "scattering axis" (the instantaneous propagation direction of the unscattered trajectory) is

$$F(\vartheta, \phi, \delta t)\, d\Omega = \frac{1}{2\pi\nu\delta t} \exp\left(-\frac{\vartheta^2}{2\nu\delta t}\right) \vartheta\, d\vartheta\, d\phi, \tag{3}$$

where $\vartheta \in [0, \pi)$ is the angle between the scattering axis and the direction of propagation of the scattered particle and $\phi \in [0, 2\pi)$ is the phase angle around the scattering axis (Torsti et al. 1996; Kocharov et al. 1998). To model the pitch-angle diffusion, we can thus pick the values of ϑ^2 and ϕ in each scattering process from exponential and uniform distributions, respectively. If the particle originally had a pitch-angle cosine μ (measured in the local solar-wind frame), the new pitch-angle cosine μ' is given by (Ellison et al. 1990)

$$\mu' = \mu \cos\vartheta + \sqrt{1-\mu^2} \sin\vartheta \cos\phi. \tag{4}$$

The geometric details of the scattering process have been described by Vainio (1998).

In the case of pitch-angle dependent scattering, the method is not as simple and efficient as in the isotropic case, because the derivatives of ν lead to additional changes in μ for each scattering process. A general method for this case can be found in Kocharov et al. (1998) and Vainio (1998), but it requires much smaller time steps than the isotropic case. Pitch-angle dependent scattering frequencies with a minimum at $\mu = 0$ are predicted by many models (e.g. Bieber et al. 1994; Ng & Reames 1995), including the standard quasi-linear theory (Jokipii 1966). Thus, it is important to include the effects of a μ-dependent ν to the scattering model. Fortunately, there is a special form of $\nu(\mu)$, which allows an efficient use of the isotropic scattering method while still capturing the essential features of reduced scattering at $\mu = 0$. Taking

$$\nu = \nu_0 \frac{|\mu|}{1+|\mu|}, \tag{5}$$

with ν_0 constant gives $D_{\mu\mu} = \frac{1}{2}\nu_0|\mu|(1-|\mu|)$, which consists of two downward-opening parabolae, in the range $\mu \in [-1, 0]$ and $\mu \in [0, 1]$, respectively. The linear dependence of ν on μ when $\mu \simeq 0$ guarantees that particles are not able to cross $\mu = 0$ by scattering, and that they remain in their initial hemisphere during each scattering process. Thus, a coordinate transformation

$$\eta = \begin{cases} 2\ (\mu - \frac{1}{2}), & \mu \geq 0 \\ \\ 2\ (\mu + \frac{1}{2}), & \mu < 0 \end{cases} \tag{6}$$

gives $\eta \in [-1, 1]$ and $D_{\eta\eta} = (d\eta/d\mu)^2 D_{\mu\mu} = \frac{1}{2}\nu_0(1-\eta^2)$. This coordinate transformation allows us to use the isotropic scattering method with a scattering frequency ν_0, with μ replaced by η, in both hemispheres.

Adding another isotropic scattering process over the full range of μ with $\nu = \epsilon\nu_0$ yields the total scattering frequency

$$\nu(\mu) = \nu_0 \left(\frac{|\mu|}{1+|\mu|} + \epsilon \right). \tag{7}$$

This means that we use Equation (3) and (4) twice, once for the η-process (with scattering rate ν_0) over one hemisphere and once for the μ process (with scattering rate $\epsilon\nu_0$) over the whole sphere. The three different components of the scattering rate (the two hemispheric processes and the one acting over the whole sphere) can be interpreted as due to different wave modes in the system and, therefore, represent different scattering processes. Thus, to the lowest order in δt, operator splitting can be applied and each scattering process can be handled separately. This simulation scheme is accurate enough to our purposes (see details in the appendix section A.1).

The functional dependence of $\nu(\mu)$ allows us to model a range of scattering conditions, from quasi-isotropic ($\epsilon \gtrsim 1$) to fully pitch-angle dependent ($\epsilon = 0$, totally decoupled hemispheres). The mean free path resulting from Equations (2) and (7) can be integrated analytically (see Appendix A.2).

Following previous works (e.g. Palmer 1982; Beeck et al. 1987; Kallenrode et al. 1993) we take the radial mean free path, λ_r, to be constant in position. Then, the mean free path parallel to the IMF line is given by $\lambda_{||} = \lambda_r \sec^2\psi$, where ψ is the angle between the field line and the radial direction, given by $\sec\psi = \sqrt{1+(r/a)^2}$, with $a = u/(\Omega_\odot \sin\Theta)$, u being the radial solar wind velocity, $\Omega_\odot$ the solar rotation rate and Θ the colatitude. Note that since λ_r and ϵ are assumed to be constant, $\lambda_{||}$ varies with position and so it does ν_0; the interdependencies of the scattering parameters are further explained in the appendix section A.3.

Additionally, the mean free path of the NR electrons is considered to be independent of the energy, in accordance with a theoretical model by Dröge (2003).

Since our aim is to compare our simulations with the *ACE* NR electron observations, the results of the model must be expressed as particle intensities at 1 AU. The method of registration consists in counting particles when they are within the interval $r \in [r_\oplus - \Delta r/2, r_\oplus + \Delta r/2]$. That means that we consider a volume $\sigma(r_\oplus)\sec\psi_\oplus\Delta r$ around the point of observation $r_\oplus$, where $\sigma(r)$ is the cross sectional area of the flux tube ($\propto B^{-1} \propto r^2\cos\psi$). This method requires that $\delta r \ll \Delta r$, in order to count each particle passing the spacecraft's position at least once. We take the flux tube cross-section as $\sigma(r) = r^2\cos\psi$ corresponding to a flux tube with a 1-sr solid angle at the solar surface. Hence, we derive the near-Earth differential intensity, i.e. the number of particles per unit time, unit energy, unit solid angle,

and unit area, given by

$$I = \frac{1}{r_{\oplus}^2} \frac{\hat{N}_{v\,\delta t}/\Delta r}{\Delta t\,\Delta E\,2\pi\Delta\mu}, \tag{8}$$

where $\hat{N}_{v\,\delta t}$ is the $E-\mu-t$ matrix of registered particles per total number of simulated particles; the subscript $v\,\delta t$ indicates that each particle has been weighted by $v\,\delta t$ when registered in the matrix (i.e., the matrix has a physical dimension of length); Δt, ΔE and $\Delta\mu$ correspond to the bin sizes of the registration matrix. Our simulations give a set of Green's functions for particle transport normalized to one particle injected per steradian at the solar surface. The energy channels and the temporal resolution are chosen according to the observational data to be compared with. The pitch-angle cosine is binned in 20 bins ($\Delta\theta = 9°$) in order to get pitch-angle distributions with high μ-resolution when $\mu \to \pm 1$. This is necessary to accomplish an accurate modeling of the angular distributions in the case of large mean free paths.

4. Fitting procedure: Deconvolution of the sectored intensities

We have developed a new technique for deconvolving the effects of interplanetary transport in order to determine the underlying time profile of particle injection near the Sun. This technique solves the inversion problem of obtaining the radial mean free path and the injection time profile at the Sun from a set of measured sectored intensities $I_l^s(t)$, where $I_l^s(t)$ is the intensity measured at time t by the sector s in the energy channel $[E_l, E_l + \Delta E_l]$. By taking into account the angular response of the EPAM/LEFS60 telescope (see Appendix B), we derive the modeled sectored intensities $M_l^s(t;\lambda_r)$, in sector s and energy interval l, that have to be compared with $I_l^s(t)$.

We consider an arbitrary function $q(t)$ -to be determined- that represents the injection function of NR electrons close to the Sun. Then, M_l^s can be written as

$$M_l^s(t;\lambda_r) = \int_{T_1}^{T_2} dt' g_l^s(t,t';\lambda_r)\, q(t'), \tag{9}$$

where $g_l^s(t,t';\lambda_r)$ represents the contribution of an impulsive injection to the modeled intensities for a given sector s and energy interval l, at a given time t, when the injection of NR electrons took place at time t', with $t' \in [T_1, T_2]$. Consequently, $M_l^s(t;\lambda_r)$ represents the modeled sectored intensities at time t, resulting from different elemental solar injections produced between T_1 and T_2. Details about the transformation of the simulated Green's function of particle propagation into $g_l^s(t,t';\lambda_r)$ functions are given in Appendix B. The calculation takes into account the angular response function of the EPAM/LEFS60 telescope and the angular directions scanned by the telescope as a function of time.

The injection energy spectrum is assumed to be a power-law, $dN_{inj}/dE = CE^{-\gamma}$, terminated by cutoff energies E_{min} and E_{max}. The energy spectrum is normalized to one particle per steradian at the solar surface, therefore, $C = (\gamma - 1)/(E_{min}^{1-\gamma} - E_{max}^{1-\gamma})$. The spectral index, γ, is estimated from the observational data. Consequently γ is not a free parameter of the model.

The dependence of g_l^s (and thus of M_l^s) on ϵ has not been explicitly shown in Equation (9), because we have not attempted to find best fit values for this parameter using a dense grid of values. Instead, we regard ϵ as a descriptor of the scattering model rather than as a free parameter.

Taking discrete values of time, we have

$$M_l^s(t_h; \lambda_r) = \sum_{j=1}^{m} g_l^s(t_h, t'_j; \lambda_r)\, q(t'_j) \tag{10}$$

where $s = 1, 2, ..., 8$ numbers the sectors of the telescope. If n_{obs} is the number of observational time points in each sector, then $t_h = t_0 + (h-1) \cdot \Delta t$, where Δt is the observational time resolution, t_0 is the origin of time of the event and $h = 1, 2, ..., n_{obs}$ numbers the observational time bins. Similarly $t'_j = T_1 + (j-1) \cdot \Delta t$, where T_1 is the time of the beginning of the injection of NR electrons ($T_1 < t_0$) and $j = 1, ..., m$ numbers the injection times.

The selection of an observational period of time for the study of the event naturally constrains the allowed time for the beginning of the injection (T_1) and its duration ($T_2 - T_1$). In the energy range $[E_{min}, E_{max}]$, the injection profile is allowed to range between

$$\begin{aligned} T_1 &= t_0 - z/v(E_{min}), \text{ and} \\ T_2 &= (t_0 + n_{obs} \cdot \Delta t) - z/v(E_{max}) \end{aligned}$$

where z is the distance along the IMF line from the source to the observer; hence $z/v(E_{min})$ corresponds to the transit time of the slowest particle considered in the analysis while $z/v(E_{max})$ is the transit time of the fastest particle.

Equation (10) can be written as

$$M_l^s(t_h; \lambda_r) \equiv M_i(\lambda_r) = \sum_{j=1}^{m} g_{ij}(\lambda_r)\, q_j = (\mathbf{g} \cdot \vec{q})_i \tag{11}$$

where $i = h + (s-1) \cdot n_{obs} = 1, 2, ..., n$ numbers the total number of observational points and $n = 8\, n_{\rm obs}$ gives the total number of observational points in all sectors; $\mathbf{g}$ is an $n \times m$ matrix with $(\mathbf{g})_{ij} = g_{ij}(\lambda_r)$.

Finally, the modeled intensities must be compared with the observations. Let b be the sector-averaged background intensity and $J_i = I_i - b$ with $I_i = I_l^s(t_h)$. We want to derive the m-vector $\vec{q}$ that minimizes the length of the n-vector $\vec{J} - \vec{M}$, that means minimizing the value of

$$||\vec{J} - \vec{M}|| \equiv ||\vec{J} - \mathbf{g} \cdot \vec{q}||,$$

subject to the constraint that $q_j \geq 0 \ \forall j = 1, 2, ..., m$. Thus, the best-fit $\vec{q} = (q_1, q_2, ..., q_m)$ corresponds to a combination of m delta-function injection amplitudes at times t_j. To obtain the best-fit values, we use the non-negative least squares (NNLS) method of Lawson & Hanson (1974), which always converges to a solution.

In addition to the injection function, the best-fit for the mean free path has also to be determined. We use the goodness-of-fit estimator

$$\zeta(\lambda_r) = \sum_{i=1}^{n} \left(\log \frac{I_i}{M_i^*(\lambda_r) + b} \right)^2 \tag{12}$$

to determine the best-fit value of λ_r. This estimator gives an equal weight of all relative residuals instead of just emphasizing the goodness of fit at the time of maximum. Here, $M_i^*(\lambda_r)$ is the best-fit model obtained from the NNLS algorithm for a given value of λ_r. The total number of independent fitting parameters is m and, thus, the number of degrees of freedom is $n - m$, which is clearly much larger than the number of model parameters, as it should be. Note that minimizing ζ implies minimizing logarithmic differences between the observational data and the modeled data.

5. The 2000 May 1 event

5.1. Electromagnetic emissions

The solar activity observed in association with the 2000 May 1 SEP event has been widely studied. The impulsive M1.1 X-ray flare with onset at 10:16 UT and maximum at 10:27 UT was the largest solar event observed on that day (Cane et al. 2002). Kahler et al. (2001) identified a compact EIT brightening in NOAA active region AR 8971 approximately at N20W54 with maximum intensity in the 10:24 UT image associated with the M1.1 flare. No accompanying Hα flare was reported. Kahler et al. (2001) also associated a fast-moving (1360 km s^{-1}) narrow ($\sim 20°$) CME with the origin of the SEP event. The CME structure was firstly seen in LASCO images above 2 $R_\odot$ at 10:54 UT (Kahler et al. 2001).

Kallenrode (2003) pointed out that narrow CMEs like this one do not necessarily correspond to the classical picture of CMEs. They rather look like jets or plasmoids that are

ejected upward from magnetic reconnection sites over active regions, which in turn might produce shock-excited radio bursts. Kallenrode (2003) suggested that the shocks associated with these narrow jet-like CMEs do not necessarily accelerate particles.

Pick et al. (2003) reported the beginning of a type III radio emission around 10:19 UT on 2000 May 1. These authors observed a series of type III metric radio sources at about the same position angle as the C2 LASCO feature, with a velocity about 1470 km s^{-1}, that extrapolated well into the height-time curve of the coronograph narrow feature. These observations were consistent with a release of energetic electrons from the corona, in the region where magnetic reconnection ejected upward the moving radio and C2 LASCO feature. Maia & Pick (2004) concluded that the SEP event on 2000 May 1 was not accompanied by a typical CME, but associated with an outward moving radio source.

Pick et al. (2006) identified the source of the 2000 May 1 SEP event from radio and optical imaging in addition to energetic ion and electron data, together with calculated coronal fields obtained from extrapolating photospheric magnetograms using the potential field source surface model (Schatten et al. 1969). Pick et al. (2006) concluded that although the narrow jet-like CME was directed $\sim$50° out of the ecliptic plane, the injected particles could promptly reach 1 AU by following the open field lines that connected the source region to the ecliptic plane. Thus, the accelerated particles were not constrained to follow the same trajectory as the bulk of the CME.

5.2. In-situ energetic particles

Figure 1 shows the spin-averaged 62–312 keV electron intensities observed by the EPAM-/LEFS60 telescope on board *ACE*. The first NR electrons were detected above the pre-event intensity background around 10:25 UT in the 175–312 keV channel (E'4). The maximum spin-averaged intensity was observed at 10:36 UT in the E'4 channel, at 10:39 UT in the 102–175 keV channel (E'3) and at 10:46 UT in the 62–102 keV channel (E'2).

The first panel in Figure 1 also includes the proton intensities observed by the LEMS120 telescope and by the ERNE telescope between 1 and 5 MeV approximately. The LEMS120 telescope is oriented 120° with respect to the spin axis, thus its look direction is opposite to the Sun. In contrast, ERNE measures particle intensities coming from the Sun within a limited field of view aligned with the nominal Parker field direction. Although these two instruments are not cross-calibrated, we are able to compare their measurements since both measured the same intensity values late in the event ($\sim$ 20:00 UT), when these profiles became almost flat. As can be seen in Figure 1, at the beginning of the event the pro-

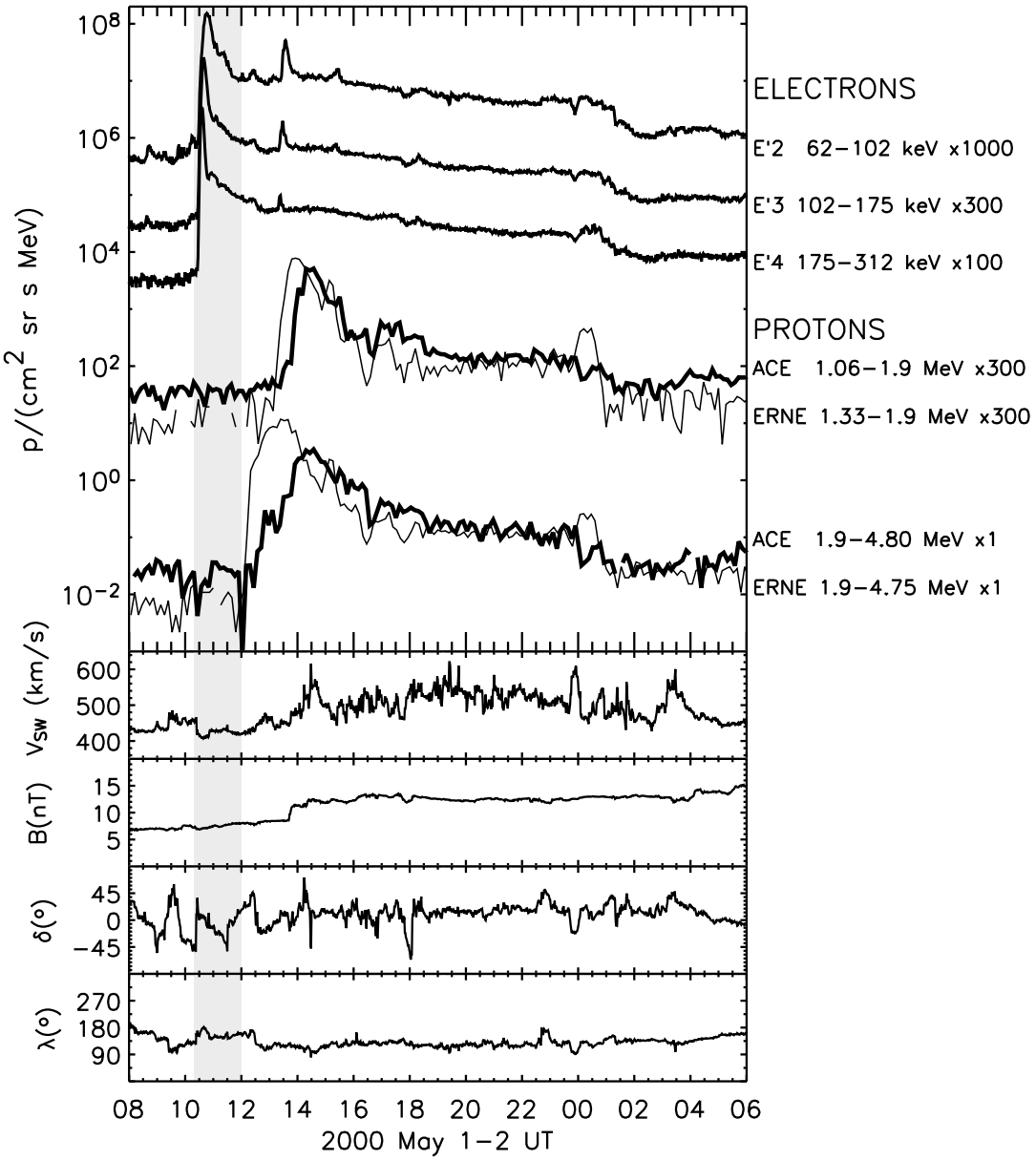

Fig. 1.— Particle event on 2000 May 1. From top to bottom: Electron and proton spin-averaged intensities observed by the LEFS60 and the LEMS120 telescopes on board *ACE*. Proton intensities observed by ERNE telescope on board SOHO are shown with a thinner line (see text for details). Solar wind velocity observed by *ACE*/SWEPAM. Magnetic field magnitude, magnetic field latitude (δ) and longitude (λ) measured by the *ACE*/MAG experiment in the RTN coordinate system. The gray area indicates the period of study of the electron event.

ton intensity profiles at the two instruments were very different, thus the event was highly anisotropic.

This SEP event displays all basic features to be classified as impulsive: high (>1) Fe/O and ^{3}He/^{4}He ratios (Mason et al. 2002), low (∼10) H/He ratios (Kahler et al. 2001) and an extremely anisotropic onset (see Figure 1 and Ho et al. 2003). The prompt phase of the NR electron event is well defined, however, as can be seen in Figure 1, the intensities of both electrons and protons remained at high levels for an extended period (∼20 h) after the flare, probably indicating a gradual injection component from the CME-driven shock.

The four lower panels in Figure 1 show the solar wind velocity, the IMF magnitude and IMF direction (δ is the latitude and λ is the longitude, in the RTN spacecraft coordinate system). The radial component of the IMF (not shown in the figure) was negative during the period of study of the event; this means that electrons coming from the Sun along the field lines had $\mu = -1$. SWEPAM data indicate that at the onset of the event *ACE* was embedded in a solar wind stream with a mean velocity of 437 km s^{-1}. Both the solar wind velocity and the IMF direction were relatively stable through the rising phase of the electron event. Therefore, the Parker IMF model and the approximations adopted in the model for particle propagation are reasonable assumptions. The nominal footpoint of the field line connecting *ACE* to the Sun was at a western longitude of 55°, as estimated from the observed solar wind speed, being close to the longitude of the flare site (W54).

In this paper, we will study the electron event observed by EPAM/LEFS60 from 10:25 UT to 12:00 UT (gray area in Figure 1). The onset of the 1.9–4.8 MeV proton event took place around 12:05 UT (Figure 1). Therefore, we have restricted the study to the period when the associated proton event had not started yet.

Since adiabatic deceleration is not important for NR electrons in the impulsive phase of the event, the spectral index γ of the electron source can be estimated by fitting a power-law to the maximum sectored intensity observed in each energy channel within the period of study of the event, following the procedure applied by Simnett (2005). The spectral index of the derived spectrum is estimated by $\gamma = 2.9$.

6. Results and discussion

We apply our model to the rising phase of the 2000 May 1 NR electron event. We consider three scattering models: isotropic scattering and two pitch-angle dependent scattering models, with $\epsilon = 0.10$ and $\epsilon = 0.01$ in Equation (7). We vary the value of the radial mean free path λ_r from 0.1 to 1.6 AU with step intervals of 0.1 AU. The calculation of the

goodness-of-fit is restricted to the time interval from 10:25 to 12:00 UT and, therefore, we force the particle injections producing an onset before 10:25 UT to be zero. Each energy channel is separately fitted and the goodness-of-fit estimator of the whole fit is obtained by adding the values obtained for each energy channel, $\zeta = \sum_l \zeta_l$.

Figure 2 illustrates the dependence of the injection profile on the radial mean free path. The five top panels show examples of the 102–175 keV electron injection profiles derived for the case with isotropic scattering, for different values of λ_r (the other cases and energies show similar behaviors). The lowest panel shows how the goodness-of-fit estimator changes as a function of λ_r. For a small λ_r, the deconvolution technique yields an impulsive injection and high ζ values. As λ_r increases, the injection profile becomes wider and the procedure gives lower ζ values. A very large λ_r increases ζ again because the prolonged injection produces high anisotropies that cannot adequately fit the intensities registered by the sectors not aligned with the IMF direction.

The adopted deconvolution technique allows us to objectively identify (within the constraints of the model) the best possible fit for all eight sectors. The lowest values of ζ obtained for each scattering case are listed in Table 1. Figure 3 shows the case with lowest ζ obtained performing the deconvolution technique. Each panel, from 1 to 8, displays the observed and modeled intensities for the three energy channels (E'2, E'3, E'4) in each sector (top) and the evolution of the pitch-angle cosine μ of the midpoint clock-angle zenith direction of the sector as a function of time (bottom). The bottom panel also shows the pitch-angle cosine range scanned by each sector as a function of time (gray area). We emphasize that for each energy channel, all eight profiles are optimized simultaneously for the whole time period.

The last panel in Figure 3 displays the omnidirectional intensities (top) and the evolution of the mean pitch-angle cosine (bottom) deduced from the model for the three modeled energy channels. The gray area displays the range of pitch-angle cosines scanned by the LEFS60 telescope as a function of time. From this figure, it can be seen that the total μ-coverage of the telescope is broad ($\sim 71\%$) during the selected period of time, which ensures a detailed

Table 1: Best goodness-of-fit estimator and the derived λ_r for each scattering model.

Scattering model	ζ {E'2, E'3, E'4}	λ_r (AU)
Isotropic	{28, 15, 17} = 60	0.8
Pitch-angle dep. ϵ=0.10	{23, 14, 13} = 50	0.9
Pitch-angle dep. ϵ=0.01	{25, 14, 10} = 49	0.9

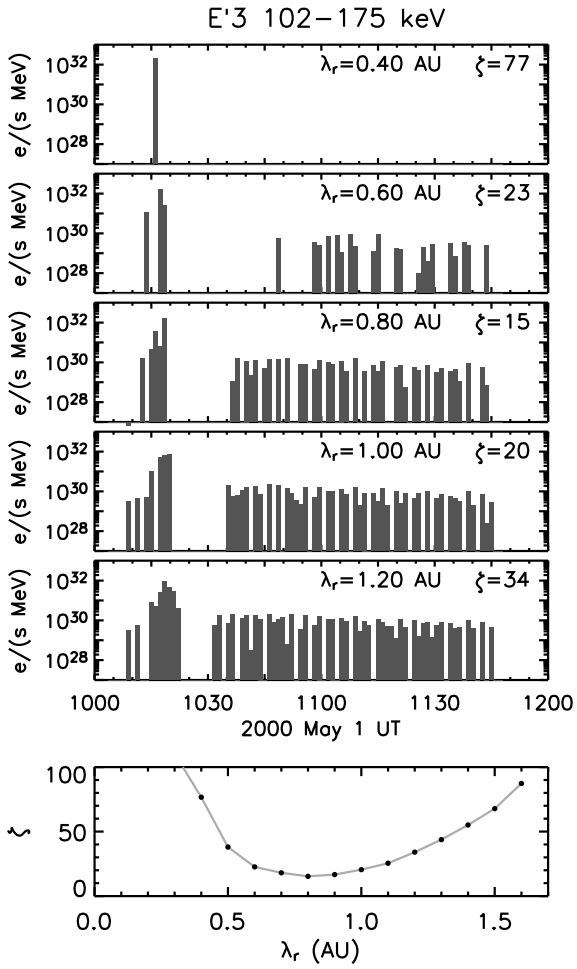

Fig. 2.— Five top panels: 102–175 keV NR electron injection profiles as a function of the radial mean free path for the case with isotropic scattering. The bottom panel displays the goodness-of-fit estimator ζ corresponding to the E'3 channel as a function of λ_r.

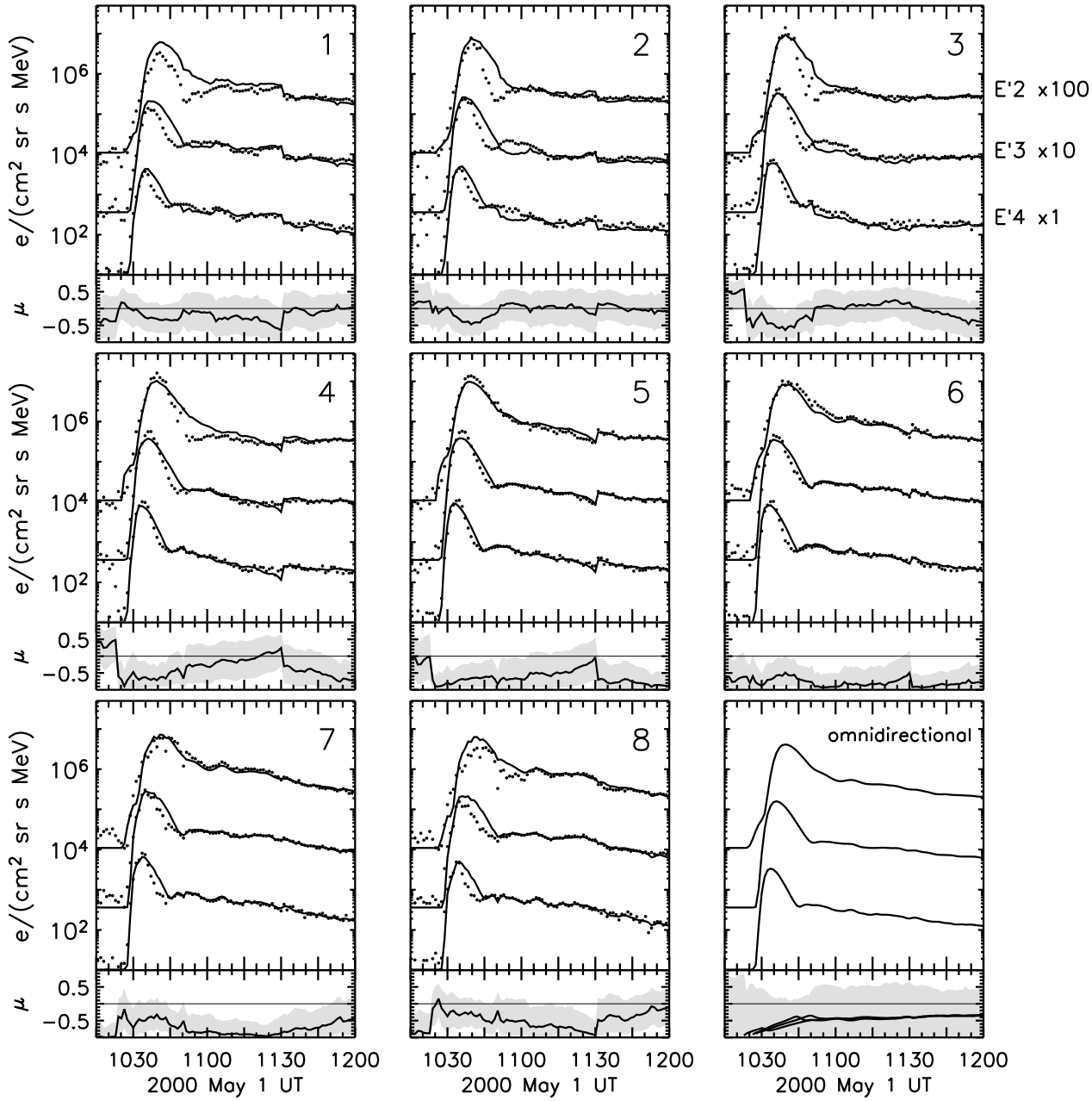

Fig. 3.— SEP event on 2000 May 1 as observed by the LEFS60 telescope on board *ACE*/EPAM. Electron sectored intensities E'4 175–312 keV, E'3 102–175 keV (×10), and E'2 62–102 keV (×100). Sectors are labeled from 1 to 8. Curves show the modeled sectored intensities and dots show the observational data. Low panels show the pitch-angle cosine of the midpoint clock-angle zenith direction of the sector (black line) and the scanned pitch-angle cosine range (gray area) as a function of time. Last panel shows the omnidirectional intensities and the mean pitch-angle cosine as a function of time deduced from the simulation. Gray area shows the pitch-angle cosine range scanned by the LEFS60 telescope.

description of the NR electron event. The LEFS60 telescope covers the forward hemisphere ($\mu \leq 0$) and part of the backward hemisphere ($0 < \mu \leq 0.5$) during most of the time (note that electrons coming from the Sun along the field lines had $\mu = -1$). However, from 10:30 to 11:10 UT the backward hemisphere is slightly scanned by the telescope.

The best fit corresponds to $\lambda_r = 0.9$ AU for the pitch-angle dependent scattering model with $\epsilon = 0.01$. The fit succeeds in reproducing most of the intensity profiles during ∼90 min. However, noticeable discrepancies between the simulated and observed sectored intensities appear in the ∼12 min following the intensity peaks. These differences are larger in the low energy channels and in the sectors not aligned with the instantaneous IMF (sectors 1, 2 and 8). One possibility that could explain these discrepancies is that the model is overestimating the scattering processes at work (i.e., the simulated particles do not propagate along of the IMF flux tube as fast as the actual electrons do). Thus, it may be possible that more involved models with a wider resonance gap near $\mu = 0$ or with a spatially varying ϵ, for example, might perform better.

The values of the solar electron injection derived from the best fit are shown in the three top panels of Figure 4 (for convenience of comparison with the observed solar electromagnetic emissions, electron injection times are shifted by 8 min to account for the light travel time). The injection profiles clearly show two components: one prompt component starting around 10:15 UT for E'2 and after 10:20 UT for E'3 and E'4 and lasting ∼5 min followed by a second weaker time-extended component starting at 10:35 UT and lasting for about ∼80 min. The total number of injected NR electrons in the whole measurement range is 3.0×10^{33}, 4.0×10^{33} or 3.8×10^{33}, as determined by the normalization of fitting the E'2, E'3 or E'4 energy channel, respectively. A large fraction ($\sim 75\%$) of the injection corresponds to the prompt injection component. At low energies (channel E'2) the prompt injection component seems to consist of two parts, separated by a few minutes. The second part (after 10:20 UT) is much larger than the first one (98% of the whole prompt component). This first small component, that the deconvolution technique yields, reflects the fact that the model does not take into account the secondary responses of the instrument to electrons of higher energy.

Haggerty et al. (2003) determined the secondary responses for the EPAM deflected electron channels and found that for hard spectra ($\gamma < 3$) DE2 and DE3 channels had strong responses to electrons of $\gtrsim$ 300 keV and $\gtrsim$ 250 keV, respectively, in addition to electrons of nominal energies (close to those of channels E'2 and E'3 of EPAM/LEFS60). The intensity profile in the rising phase of the event in E'2 is different from the other two higher energy channels (Figure 3) and is typical of secondary responses due to higher-energy electrons arriving at 1 AU faster than the electrons corresponding to the nominal energy window of E'2. Therefore, we assume that the actual prompt component injection is just

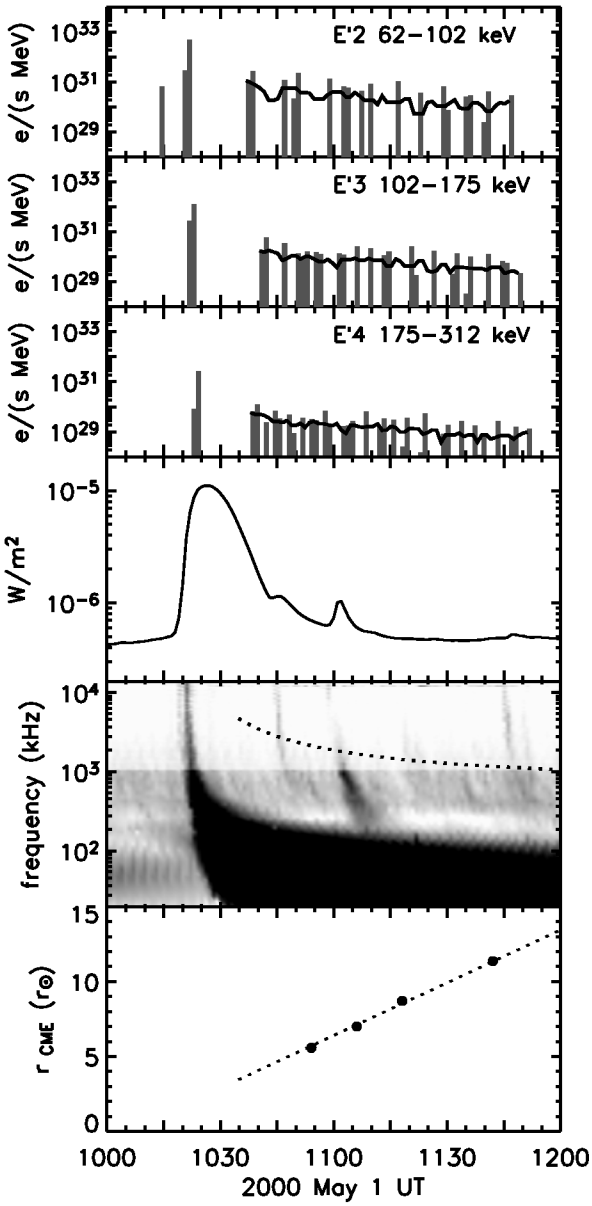

Fig. 4.— From top to bottom: NR electron injection profiles derived by the deconvolution technique for the three modeled energy channels (injection times are shifted by 8 min to account for the light travel time). In addition to the fit result (histogram), smoothed curves obtained by 6-point moving averaging are shown. 1-8 Å X-ray flux observed by *GOES-8*/XRS. Radio flux observed by *WIND*/WAVES. Dotted line shows the local electron plasma frequency at the height of the CME leading edge (Mann et al. 1999). Height-time plot of the CME leading edge from the *SOHO*/LASCO Catalog.

the second part of this profile, starting after 10:20 UT in the E'2 energy channel.

The second injection component appears patchy. This is probably due to the deconvolution method, since it tries to cope with fluctuating fluxes by temporally switching on and off the injection, although the fluctuations are more probably related to the spacecraft crossing magnetic flux tubes with different transport conditions and/or injection histories. This is why we plot in the three top panels of Figure 4 smoothed curves for the second injection component, calculated using a 6-point moving average. It is worth noting that by convolving the modeled Green's functions by the smoothed injection profile, the obtained sectored intensities do not practically differ from the ones obtained for the patchy injection profile ($\zeta \simeq 49$).

By integrating the injection function over time for each energy channel, we can construct the time-integrated spectrum which corresponds to a piecewise normalized power-law spectrum with the assumed spectral index of $\gamma = 2.9$ in each energy channel. As the total number of electrons in the E'2 channel is a bit lower than what the assumed spectral index would demand, the spectrum can be best fit by a single power-law index if we take $\gamma = 2.7$. We find good agreement between the spectral index deduced from the time-integrated spectrum and the one estimated from the observations.

The three lower panels of Figure 4 compare the timing of the electron injection with the electromagnetic emissions observed at 1 AU. These plots show, from top to bottom, the soft X-ray flux observed by *GOES*/XRS, the radio flux observed by *WIND*/WAVES and the CME height-time plot obtained from the *SOHO*/LASCO Catalog[3]. Neglecting the first part of the prompt electron injection in E'2 at 10:15 UT (probably related to secondary responses of this energy channel), the start of the prompt electron injection in E'2 coincides with the start of the X-ray flare. Comparing the times of the maximum injection to the electromagnetic emissions, we see that the time of maximum injection at the highest energies coincides with the maximum intensity of the X-ray emission. Moreover, the timing of the type III burst is consistent with the start of the prompt injection in E'2.

The timing of the delayed injection component is a bit more uncertain since its beginning is still masked under the tail of the prompt component. It seems to start earlier than the second type III burst in Figure 4, which coincides with a small peak in the soft X-ray intensity around 10:46 UT. However, as the region near the minimum of the goodness-of-fit estimator $\zeta(\lambda_r)$ providing acceptable fits is rather extended, the actual value of the mean free path may be a bit smaller than the best-fit value. In this case, the delayed injection starts later than in the best-fit case and may coincide with the second type III burst. Interestingly, the

[3]http://cdaw.gsfc.nasa.gov

third type III burst, starting right after 11:00 UT (and also related to a soft X-ray peak), is consistent with it originating from a source at a height of the CME leading edge if the density model of Mann et al. (1999) is used (dotted line in the fifth panel of Figure 4). Some faint fast-drifting radio bursts near 11:20 UT and 11:35 UT seem to originate from the CME leading edge as well. Maia & Pick (2004) already pointed out that the position of these successive type III-like radio sources extrapolate well into the height-time curve of the CME. This supports a scenario, where the source of the second injection is, at least partly, provided by the CME-driven shock.

7. Conclusions

We have developed a Monte Carlo model to efficiently and accurately simulate interplanetary NR electron transport including adiabatic focusing, pitch-angle dependent scattering, and solar-wind effects. We have also developed a simplified model of the angular response of the EPAM/LEFS60 telescope on-board *ACE* suitable for transforming the pitch-angle distributions obtained as a result of the Monte Carlo simulations to sectored intensities measured by the telescope. Finally, we have presented a deconvolution method to deduce from the observed sectored intensities the best-fit transport conditions and the injection profile of NR electrons.

The presented method has been applied to the impulsive SEP event on 2000 May 1, associated with an impulsive X-ray flare, type III radio bursts, and a narrow jet-like fast CME. The deconvolved transport conditions reveal a radial mean free path of 0.9 AU with pitch-angle dependent scattering. The eight observed sectored intensities are fitted in detail for more than 90 min, except for a short period ($\sim$12 min) right after the time of peak intensities where observed intensities remain below the modeled intensities. This discrepancy may suggest that the assumed scattering model performs more efficiently than the actual scattering processes at work. The resulting injection profile consists of two main components, a prompt component lasting 2–3 min and probably related to a type III radio burst observed by *WIND*/WAVES at $\sim$10:21 UT, and a delayed component starting at the Sun around 10:35 UT with a typical injection decay time scale of $\sim$0.5 h. The delayed component may be at least partly supplied by particle acceleration at the CME-driven shock.

By using this new technique, we have been able to derive, the onset, intensity and duration of the injection of NR solar electrons, without any a priori assumption about the functional form of the particle injection profile.

NA and BS acknowledge the financial support of the Ministerio de Ciencia y Tecnología

(Spain), under the projects AYA2004-03022 and AYA2007-60724. Partial computational support has been provided by the Centre de Supercomputació de Catalunya (CESCA). DL was partially supported by NASA under grants NAG5-10787, NAG5-13487 and NSF under research grant ATM-0648181. We wish to thank the *SOHO*/ERNE and *ACE*/EPAM teams for making their data available. NA wishes to thank A. Vourlidas for valuable discussions concerning this work.

A. Monte Carlo simulations of interplanetary transport

A.1. Steady-state solution of the Fokker-Planck equation

The simulation scheme used in this paper (Section 3) has been verified by checking that the Monte Carlo technique reproduces the analytical steady-state solution of the Fokker-Planck equation for the spatially integrated pitch-angle distribution, $F(\mu) = dN/d\mu$. In this case, the Fokker-Planck equation to be solved is

$$\frac{\partial}{\partial\mu}\left(\frac{1-\mu^2}{2L}vF\right) = \frac{1}{2}\frac{\partial}{\partial\mu}\left((1-\mu^2)\nu\frac{\partial F}{\partial\mu}\right). \tag{A1}$$

For a system with constant focusing length, L, the integration of this equation yields

$$F(\mu) = F_0 \exp\left(\frac{v}{L}\int_0^\mu \frac{d\mu'}{\nu}\right) \tag{A2}$$

as a time asymptotic state of a corresponding simulation. The comparison of such analytical distributions with the distributions obtained by the Monte Carlo simulations for the three scattering models show good agreement. As an example, Figure 5 shows the isotropic scattering case and the pitch-angle dependent scattering case with $\epsilon = 0.10$. The code was run with $L = \lambda_{||} = 0.5$ AU and simulation running time $t = 100L/v$, enough to reach the steady-state.

A.2. Analytical expression of the mean free path for a pitch-angle dependent scattering model

The motion of solar energetic particles (SEPs) from the Sun to the Earth is generally considered to be well understood in terms of the transport processes of pitch-angle scattering (Jokipii 1966; Bieber et al. 1994; Dröge 2003), adiabatic focusing (Roelof 1969), solar wind convection, and adiabatic deceleration (Ruffolo 1995; Kocharov et al. 1998).

In the solar wind frame, the pitch-angle diffusion coefficient is given by Equation (1). For isotropic scattering, the scattering frequency is constant ($\nu = \nu_0$) and $\lambda_{||} = v/\nu_0$. For a pitch-angle dependent scattering model we adopt $\nu(\mu)$ as given by Equation (7), where the ϵ parameter allows us to define different levels of scattering at $\mu = 0$. Then, the parallel mean free path can be expressed in terms of ν_0 and ϵ, as

$$\lambda_{||} = \frac{3v}{4} \int_{-1}^{+1} \frac{1-\mu^2}{\nu(\mu)} d\mu = \frac{v}{\nu_0} \phi(\epsilon) \tag{A3}$$

where $\phi(\epsilon)$ has the analytical form

$$\phi(\epsilon) = \frac{3}{2} \int_0^1 \frac{1-\mu^2}{\frac{\mu}{1+\mu} + \epsilon} d\mu = \frac{1}{4(1+\epsilon)^4} \left[4\epsilon^3 + 15\epsilon^2 + 12\epsilon + 1 + 6(1+2\epsilon) \ln\left(\frac{1+2\epsilon}{\epsilon}\right) \right] \tag{A4}$$

Figure 6 displays the isotropic pitch-angle diffusion coefficient versus the pitch-angle cosine for $\lambda_{||} = 0.5$ AU, together with the diffusion coefficient of two pitch-angle dependent scattering models defined by $\epsilon = 0.10$ and $\epsilon = 0.01$. From this figure, it can be seen that in these two latter models $D_{\mu\mu}$ reaches its maximum value around $\mu \sim \pm 0.5$ and that $D_{\mu\mu}(\mu = 0) \neq 0$. Note that when $\mu \sim 0$, $D_{\mu\mu}$ has larger values for $\epsilon = 0.10$ than for $\epsilon = 0.01$.

We use the mean free path for the parametrization of the scattering frequency in the Monte Carlo model. For a given pitch-angle dependent scattering model with a certain ϵ, the level of diffusion can be adjusted by changing the value of ν_0, which is derived from the value of the $\lambda_{||}$. Since λ_r is assumed to be constant, $\lambda_{||}$ increases with radial distance. Figure 7 plots the values $\lambda_{\|}$ and the focusing length, L, for $\lambda_r = 1$ AU.

A.3. Mean free path under weak scattering conditions

The strong magnetic focusing effect close to the Sun makes that the initially injected distribution of SEPs become a beamlike anisotropic distribution shortly after its release near the Sun. Thus, SEP events usually show highly anisotropic distributions during their initial phase with the average pitch-angle cosine of the particles remaining close to $|\mu| = 1$ (outwards). The relationship between the pitch-angle diffusion coefficient $D_{\mu\mu}$ and the mean free path $\lambda_{||}$ given in Equation (2) is valid in the case of strong scattering and thus isotropic pitch-angle distributions. Under weak scattering conditions, the mean free path only gives a crude measure of the scattering strength. In this case, specific functions describing the pitch-angle diffusion coefficients should be given, in particular in the range close to $\mu \sim 1$.

We can define a phenomenological scattering length to illustrate the strength of scattering near $|\mu| = 1$ as $\lambda_1(r) = v/\nu(1, r) \approx 2v/\nu_0$. Figure 7 plots the values of λ_1 as a function

of distance for the two scattering models ($\epsilon = 0.10$ and 0.01). (Note that for the isotropic model, $\lambda_1 = \lambda_{||}$.) For the two pitch-angle dependent scattering models, the scattering length λ_1 gives an estimate of the beam isotropization length within a single hemisphere, whereas $\lambda_{\|}$ is more related to the scattering rate across $\mu = 0$.

B. Sectored intensities computed by a particle telescope on board a spin-stabilized spacecraft

B.1. Angular response model of the EPAM/LEFS60 sectors

In order to model the sectored data collected by the LEFS60 telescope of the EPAM experiment (Gold et al. 1998), it is necessary to derive the angular response function of the sectors of the telescope. The model developed in this paper includes the essential parts of the geometry of the detector system but it does not take into consideration other factors as the effects of electron scattering in the collimated aperture. The angular response is obtained by analyzing how an isotropic population of particles is seen by each one of the eight sectors of the LEFS60 telescope.

We take X, Y, Z as the coordinate system where the Z axis is aligned with the ACE spin vector and the X and Y axes are perpendicular to it, maintaining constant orientation with respect to the ecliptic plane. The clock-angle ϕ is the azimuth angle measured around Z from the positive X toward the positive Y, and the spin-pitch angle ξ is the polar angle of this coordinate system. We refer to the coordinate system of the LEFS60 telescope as X', Y', Z'. The Z' axis is oriented toward the zenith direction of the telescope. Figure 8 illustrates these two coordinate systems. As the spacecraft spins, the zenith direction changes at constant angular velocity with an uniformly increasing clock-angle $\phi_0(t) \propto t$ and a constant spin-pitch angle $\xi_0 = 60°$. The azimuth angle in this system, ϕ', is measured around the Z' axis from the positive X' toward positive Y' and the polar angle, ξ', is the zenith angle of a particle incident on the telescope.

We model the LEFS60 telescope as a conical aperture with an effective view-cone half-width of $\xi'_{\max} = 25°$, mounted on a spinning spacecraft with a zenith direction given by a spin-pitch angle of $\xi_0 = 60°$. In fact, the view cone of LEFS60 has a full width of 53°, but we use a slightly smaller value because the response in a real collimated aperture decreases over a range of zenith angles, instead of abruptly going to zero at the edge.

The response function R_{jk} of each sector is represented by a bi-dimensional matrix, where each element (j, k) represents the probability per square degree that a particle with direction $(\xi, \phi) \in [j\alpha, (j+1)\alpha] \times [k\alpha, (k+1)\alpha]$, with $\alpha = 1°$, is detected by the telescope

when its zenith axis sweeps a 45°-wide clock-angle sector. Thus, we take $\xi \in [0°, 180°]$ and $\phi \in [0°, 360°)$, that is, $j \in [0, 179]$ and $k \in [0, 359]$. Thus, R_{jk} is a 180×360 matrix.

We start by simplifying the problem and calculating the response function of a sector centered at $(\xi_0, \phi_0) = (60°, 0°)$. Assuming a non-rotating telescope, we generate a large number of isotropic particle trajectories incident on the detector. We take the squared zenith angle cosines, $\cos^2 \xi'_i$, uniformly distributed between the squared cosine of the view-cone half-width, $\cos^2 \xi'_{\max}$, and 1, and the azimuth angles ϕ'_i uniformly distributed between 0 and 2π. The subscript i identifies the generated trajectories. For each trajectory (ξ'_i, ϕ'_i), we then calculate the spin-pitch angle of the trajectory, ξ_i, which is given by

$$\cos \xi_i = \sin \xi_0 \sin \xi'_i \cos \phi'_i + \cos \xi'_i \cos \xi_0 \tag{B1}$$

and the respective clock-angle, ϕ_i, by

$$\sin \phi_i = \frac{\sin \xi'_i}{\sin \xi_i} \sin \phi'_i. \tag{B2}$$

The next step is to take into account the sampling of clock-angle of the detector-zenith direction as the spacecraft spins. We do this by adding to the clock-angle ϕ_i a random number uniformly distributed between (-$\delta\phi$/2, $\delta\phi$/2) with $\delta\phi = 45°$. The result is a set of particle trajectories drawn from an isotropic particle distribution, as seen by the detector when its zenith axis sweeps a 45°-wide clock angle sector centered at $\phi_0 = 0°$.

We create the response matrix R_{jk} of the sector by binning the particle trajectories (ξ_i, ϕ_i) on the matrix R_{jk} and normalizing to unity, $\sum_{jk} R_{jk} = 1$. Figure 9 illustrates the response function of this sector. Note that it is not a boxcar function, but it peaks at the midpoint clock-angle zenith direction of the sector.

Finally, the response function of each of the eight EPAM/LEFS60 sectors can be derived by just shifting R_{jk} in clock-angle, taking into account that the midpoint clock-angle of the first sector is located at 67.5° and is separated by a multiple of 45° from the neighboring sectors (Gold et al. 1998).

B.2. Sectored Green's functions

Once we know the response function of the EPAM/LEFS60 sectors, it is possible to transform simulated differential intensities into modeled sectored intensities, which are directly comparable with observations. We calculate the pitch-angle cosine matrix $\mu_{jk}(t) = \mu(\xi_j, \phi_k, \vec{B})$ for the same grid of directions (ξ, ϕ) as was used for the calculation of R_{jk}. Note

that this matrix changes as a function of time due to the change of direction of the magnetic field vector, $\vec{B}(t)$. From this $\mu_{jk}(t)$ matrix, we can calculate the corresponding angular distribution $G_l(\mu_{jk}(t), t)$, where $G_l(\mu, t)$ are the simulated pitch-angle distributions in the energy range $[E_l, E_l + \Delta E_l]$ resulting from an impulsive injection at $t = 0$. In this case, the modeled intensities in sector s and energy channel l are given by

$$g_l^s(t) = \sum_{jk} R_{jk}^s \; G_l(\mu_{jk}(t), t); \tag{B3}$$

i.e. the product is performed element by element and the sum extends over all (ξ, ϕ) directions.

In general, we can write

$$g_l^s(t, t') \;\; = \;\; \int_0^{\pi} d\xi \int_0^{2\pi} d\phi \, R^s(\xi, \phi) \; \frac{1}{\Delta E_l} \int_{E_l}^{E_l + \Delta E_l} dE \, G(\mu(\xi, \phi, t), t - t', E), \tag{B4}$$

where $g_l^s(t, t')$ represents the modeled intensity, for a given sector s and energy channel l, at a given time t, when the injection of NR electrons took place at time t'.

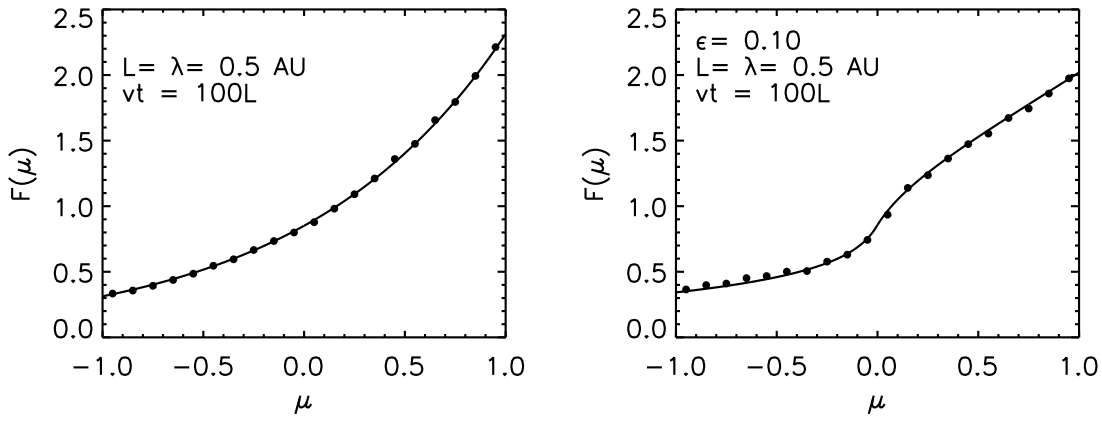

Fig. 5.— Simulated (dotted) and analytical (line) normalized steady-state pitch-angle distributions for a system with constant focusing length and isotropic scattering (*left*) or pitch-angle dependent scattering with $\epsilon = 0.10$ (*right*).

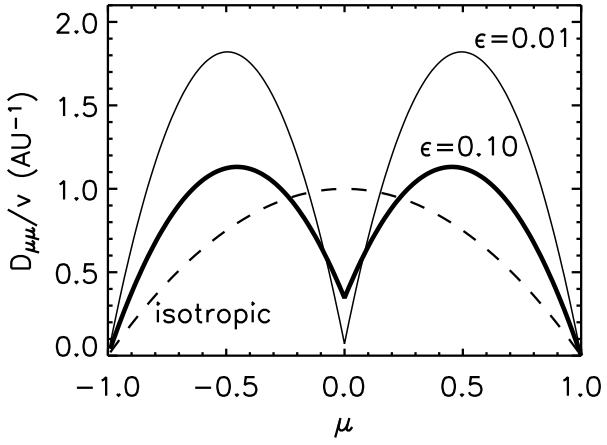

Fig. 6.— $D_{\mu\mu}$ versus μ for $\lambda_{||} = 0.5$ AU; isotropic (dashed line) and pitch-angle dependent cases with $\epsilon = 0.10$ (thick line) and $\epsilon = 0.01$ (thin line).

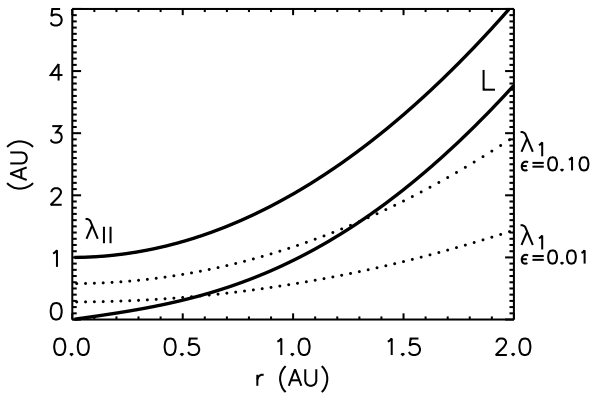

Fig. 7.— Focusing length, L, and parallel mean free path, $\lambda_{||}$, for a constant radial mean free path $\lambda_r = 1.0$ AU. Dependence of the scattering length, λ_1, on the radial distance for the pitch-angle dependent scattering models with $\epsilon = 0.10$ and $\epsilon = 0.01$ (dotted lines).

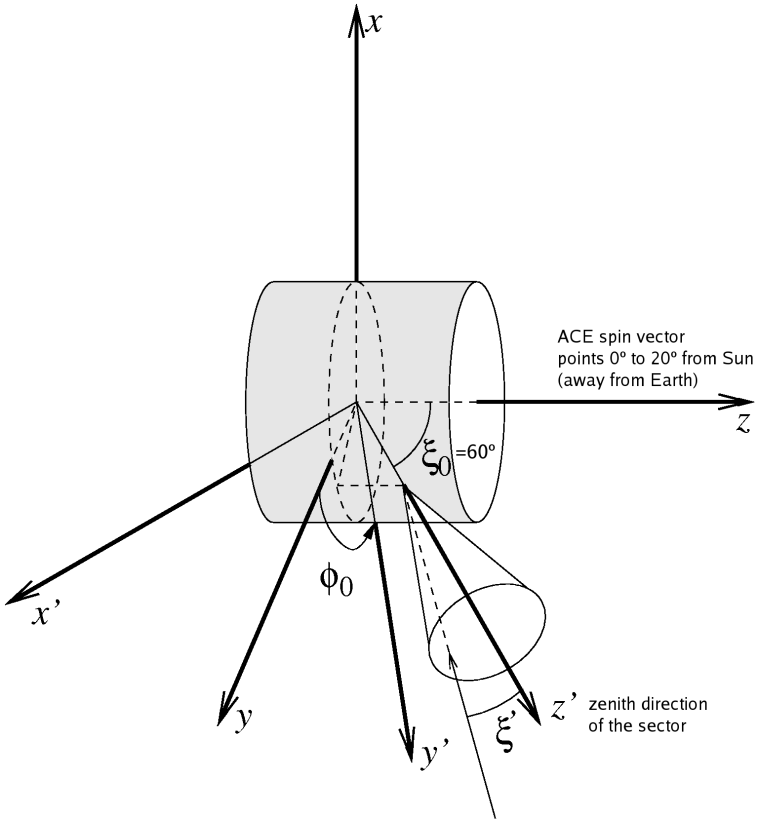

Fig. 8.— Coordinate systems: X, Y, Z denote the coordinate system where Z is aligned with the ACE spin vector and X and Y axes are perpendicular to it. The spin-pitch angle ξ is the polar angle of this coordinate system. X', Y', Z' denote the coordinate system of the LEFS60 telescope. The Z' axis is oriented toward the zenith direction of LEFS60 ($\xi_0 = 60°$). See text for details.

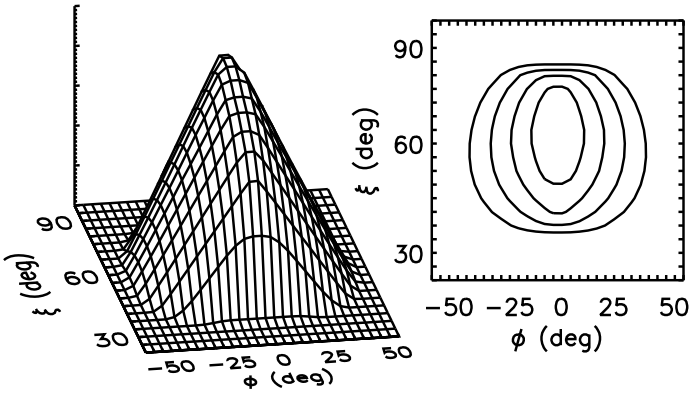

Fig. 9.— Bidimensional response function for a sector characterized by a midpoint clock-angle of 0°, a view cone full-width of 50°, a clock-angle sector size of 45°, and a spin-pitch angle of 60°. Surface plot (left) and contour diagram (right).

REFERENCES

Aurass, H., Vrsnak, B., & Mann, G. 2002, A&A, 384, 273

Beeck, J., Mason, G.M., Hamilton, D.C., Wibberenz, G., Kunow, H., Hovestadt, D., & Klecker, B. 1987, ApJ, 322, 1052

Bieber, J.W., Matthaeus, W.H., Smith, C.W., Wanner, W., Kallenrode, M., & Wibberenz, G. 1994, ApJ, 420, 294

Bougeret, J.L., et al. 1995, Space Sci. Rev., 71, 5

Brueckner, G.E., et al. 1995, Sol. Phys., 162, 357

Cane, H.V., Erickson, W.C., & Prestage, N.P. 2002, J. Geophys. Res., 107, 14

Cane, H.V. 2003, ApJ, 598, 1403

Cliver, E.W., & Ling, A.G. 2007, ApJ, 658, 1349

Ellison, D.C., Jones, F.C., & Reynolds, S.P. 1990, ApJ, 360, 702

Dröge, W. 2003, ApJ, 589, 1027

Gold, R.E., et al. 1998, Space Sci. Rev., 86, 541

Haggerty, D.K., & Roelof, E.C. 2002, ApJ, 579, 841

Haggerty, D.K., & Roelof, E.C. 2003, Adv. Space Res., 32, 423

Hasselmann, K., Wibberenz, G. 1968, Z. Geophys., 34, 353

Hasselmann, K., Wibberenz, G. 1970, ApJ, 162, 1049

Ho, G.C., Roelof, E.C., Mason, G.M., Lario, D., & Mazur, J.E. 2003, Adv. Space Res., 32, 2679

Jokipii, J.R. 1966, ApJ, 146, 480

Kahler, S.W., Reames, D.V., & Sheeley, N.R. Jr 2001, ApJ, 562, 558

Kahler, S.W., Aurass, H,, Mann, G., & Klassen, A. 2007, ApJ, 656, 567

Kallenrode, M.B., Wibberenz, G., & Hucke, S. 1992, ApJ, 394, 351

Kallenrode,M.B. 2003, J. Phys. G.: Nucl. Part. Phys., 29, 965

Klein, K.L. & Posner, A. 2005, A&A, 438, 1029

Kocharov, L., Vainio, R., Kovaltsov, G. A., & Torsti, J. 1998, Sol. Phys., 182, 195

Krucker, S., Larson, D.E., Lin, R.P., & Thompson, B.J. 1999, ApJ, 519, 864

Lawson, C.L., & Hanson, R.J. 1974, Solving Least Squares Problems (Englewood Cliffs: Prentice-Hall)

Lin, R.P. 1970, Sol. Phys., 12, 266

Liu, S., Petrosian, V., Mason, G.M. 2006, ApJ, 636, 462

Maia, D.J.F., & Pick, M. 2004, ApJ, 609, 1082

Maia, D.J.F., Gama, R., Mercier, C., Pick, M., Kerdraon, A., & Karlický, M. 2007, ApJ, 660, 874

Mann, G., Jansen, F. , MacDowall, R.J., Kaiser, M.L., & Stone, R.G. 1999, A&A, 348, 614

Mason, G.M., et al. 2002, ApJ, 574, 1039

McComas, D.J., Bame, S.J., Barker, P., Feldman, W.C., Phillips, J.L., & Riley, P. 1998, Space Sci. Rev., 86, 563

Ng, C.K., & Reames, D.V. 1995, ApJ, 453, 890

Palmer, I.D. 1982, Rev. Geophys. Space Phys., 20, 335

Parker, E.N., 1958, ApJ, 128, 664

Petrosian, V., & Liu, S. 2004, ApJ, 610, 550

Pick, M., Mason, G.M., Wang, Y.M., Tan, C., & Wang, L. 2006, ApJ, 648, 1247

Pick, M., Maia, D., Wang, S.J., Lecacheux, A., & Hawkins III, S.E. 2003, Adv. Space Res., 32, 2527

Qin, G., Zhang, M., Dwyer, J.R., Rassoul, H.K., & Mason, G.M. 2005, ApJ, 627, 562

Reames, D.V. 1999, Space Sci. Rev., 90, 413

Roelof, E.C. 1969, in Lectures in High Energy Astrophysics, ed. H. gelmann & J. R. Wayland (NASA SP-199; Washington: NASA), 111

Ruffolo, D. 1995, ApJ, 442, 861

Schatten, K.H., Wilcox, J.M., & Ness, N.F. 1969, Sol. Phys., 6, 442

Simnett, G.M., Roelof, E.C., & Haggerty, D.K. 2002, ApJ, 579, 854

Simnett, G.M. 2005, Sol. Phys., 229, 213

Smith, C.W., L'Heureux, J., Ness, N.F., Acuna, M.H., Burlaga, L.F. & Scheifele J. 1998, Space Sci. Rev., 86, 613

Torsti, J., et al. 1995, Sol. Phys., 162, 505

Torsti, J., Kocharov, L.G., Vainio, R., Anttila, A., & Kovaltsov, G. A. 1996, Sol. Phys., 166, 135

Vainio, R. 1998, Ph.D. thesis, University of Turku (Finland)

Wang, L., Lin, R.P., Krucker, S. & Gosling, J.T. 2006, Geophys. Res. Lett., 33, L03106, doi:10.1029/2005GL024434